Numerical analysis of direct-current microdischarge for space propulsion applications using the particle-in-cell/Monte Carlo collision (PIC/MCC) method

Reference:
Kong Linghan, Wang Weizong, Murphy Anthony B., Xia Guangqing.- Numerical analysis of direct-current microdischarge for space propulsion applications using the particle-in-cell/Monte Carlo collision (PIC/MCC) method
Journal of physics: D: applied physics - ISSN 0022-3727 - 50:16(2017), 165203
Full text (Publisher's DOI): https://doi.org/10.1088/1361-6463/AA623F
To cite this reference: http://hdl.handle.net/10067/1436420151162165141

Numerical analysis of direct-current microdischarge for space propulsion applications using the Particle-In-Cell/Monte Carlo Collision (PIC/MCC) method

Numerical Analysis of Direct-Current Microdischarge for Space Propulsion Applications using the Particle-In-Cell/Monte Carlo Collision (PIC/MCC) Method

Linghan Kong[1, 2] *, Weizong Wang[1, (a)] *, Anthony B Murphy[3] and Guangqing Xia[4]

1. Qian Xuesen Laboratory of Space Technology, China Academy of Space Technology, Beijing 100094, China
2. School of Aerospace, Tsinghua University, Beijing, 100084, China
3. CSIRO Manufacturing, PO Box 218, Lindfield NSW 2070, Australia
4. State Key Laboratory of Structural Analysis for Industrial Equipment, Dalian University of Technology, Dalian 116024, China

E-mail: wangweizong@gmail.com, tony.murphy@csiro.au

* These authors contributed equally to this work

(a) Author to whom any correspondence should be addressed

Abstract: Microdischarges are an important type of plasma discharge that possess several unique characteristics, such as presence of a stable glow discharge, high plasma density and intense excimer radiation, leading to several potential applications. The intense and controllable gas heating within the extremely small dimensions of microdischarges has been exploited in micro-thruster technologies by incorporating a micro-nozzle to generate the thrust. This kind of micro-thruster has a significantly improved specific impulse performance compared to conventional cold gas thrusters, and can meet the requirements arising from the emerging development and application of micro-spacecraft. In this paper, we performed a self-consistent two-dimensional particle-in-cell simulation, with a Monte Carlo collision model, of a microdischarge operating in a prototype micro-plasma thruster with a hollow cylinder geometry and a divergent micro nozzle. The model takes into account the thermionic electron emission including the Schottky effect, the secondary electron emission due to cathode bombardment by the plasma ions, several different collision processes, and a non-uniform argon background gas density in the cathode–anode gap. Results in the high-pressure (several hundreds of torr), high-current (mA) operating regime showing behavior of the plasma density, potential distribution, and energy flux towards the hollow cathode and anode are presented and discussed. In addition, the results of simulations showing the effect of different argon gas pressures, cathode material work function and discharge voltage on the operation of the microdischarge thruster are presented. Our calculated properties are compared with experimental data under similar conditions and qualitative and quantitative agreements are reached.

Keywords: Electric propulsion; Microdischarge; Particle simulation; Non-equilibrium plasma

Submitted to *Journal of Physics D: Applied Physics*

[(a)] Current address: University of Antwerp, BE-2610 Wilrijk-Antwerp, Belgium.

1. Introduction

Satellites play a critical role in many modern applications and systems; for example, they are used for communication purposes [1], global positioning systems [2], weather and climate monitoring [3] and astronomical research [4]. In recent years, smaller micro-spacecraft, on the scale of tens of kilograms, have been widely exploited in industrial, military, and scientific space missions. Their advantages over conventional large complex satellites include small volume, light weight and low launch costs, which result in improved reliability and flexibility. To complement the rapid development and growing implementation of micro-satellites, new types of micro-thrusters with corresponding properties, including light weight, small volume, high efficiency and reliable micro-propulsion systems, are urgently needed [4]. Use of conventional cold gas propulsion and chemical propulsion methods for micro-thrusters has a large disadvantage of low specific impulse performance, which greatly reduces their potential for applications [5]. Therefore, development of a highly-efficient and reliable propulsion technique, and scaling down the power and size of the thruster systems to suit the requirements of micro-satellites, are still significant scientific and engineering challenges [6]-[9].

Electric propulsion, which is less expensive and provides higher specific impulse and higher control precision than conventional methods, has recently become one of the most promising micro-propulsion methods [10]. The development and applications of electric propulsion systems are closely linked with the advancement of plasma technology [11]. One type of plasma that has attracted substantial recent interest is the microdischarge, its ability to produce stable glow discharges, intense gas heating and large numbers of active particles has motivated research into potential applications such as nanomaterial synthesis, thin film coating, sterilization, materials processing and implementation in plasma displays and as a light source [12]. The intense and controllable gas heating within the extremely small dimensions of microdischarges has been exploited in micro-propulsion technologies. A new micro-thruster concept, known as the Micro Plasma Thruster (MPT), has been proposed and investigated; it combines a diverging exit nozzle with a micro-hollow cathode discharge (MHCD) passage [13]-[16]. The propellant gas passes through the discharge area and is preheated by the discharge, resulting in a significant increase of the specific impulse.

The small geometric dimensions in MPT have limited detailed quantitative experimental diagnostic studies of their properties, although some examples of such studies have been performed in the literature [14], [17]-[18]. Acquiring the detailed electron and ions kinetic information are also very challenging experimentally. Computer simulation is, however, a useful tool to reveal the physical and chemical characteristics of microdischarges. In previous studies, Raja and co-workers established a detailed computational model of direct current argon and helium discharges that self-consistently coupled the plasma phenomena with the high-speed flow. The model described the steady microdischarge power deposition behaviour, the plasma dynamics, the gas-phase chemical kinetics and the overall propulsion system performance in both a simplified cylindrical-channel geometry with hollow (annular) electrodes [19] and a prototypical MPT device with divergent exit nozzle [20]. The results of these investigations indicated that an increase in input electrical power results in an almost linear increase in the gas temperature, and underlined the promise of the MPT concept for small satellite propulsion. The fluid models used in these studies of the discharge characteristics of the MPT provide a valuable description of the plasma. However, they did not account for kinetic effects that can occur close to the cathode due to the deviations of the particle distribution functions from a Maxwellian distribution. This could increase the electron–neutral collision rate coefficients, thereby affecting the plasma parameters [21]. In order to obtain kinetic information that is not available from fluid models, Particle-in-Cell simulations with a Monte-Carlo collision model (PIC–MCC) have been widely employed in the analysis of microplasmas [22]-[30], including several studies concerned with MHCDs [24]-[30]. However, there have been no published studies of PIC/MCC simulations of MHCDs in a real MPT geometry, that is, with a divergent exit nozzle to generate thrust. Previous PIC–MCC studies of MHCDs showed that the discharge properties strongly depend on the initial operating parameters. For example, when the operating pressure is low enough that the electron mean free path exceeds the inner diameter of discharge passage, the electrons emitted from the cathode will experience oscillations in the potential well produced by the positive ions. The oscillations can give the electrons sufficient energy to excited and ionize the neutral species [31]. This means that a high density plasma can be obtained in the MHCD. When the background pressure is higher, the electron mean free path is less then or comparable to the diameter of the discharge passage. The acceleration by the voltage fall in the cathode sheath becomes dominant in sustaining the discharge. In a real MPT device, the pressure experiences a large drop from hundreds or tens of Torr at the inlet to an extremely low pressure close to the vacuum space at the outlet. Therefore, the influence of the non-uniform distribution of background pressure on the MHCD behaviour should be taken into account. Additionally, the existence of the divergent exit nozzle can influence the distribution of electric potential and hence the discharge processes, so their role in the development of MHCD in MPT has also to be clarified.

In this paper, the evolution of a microdischarge in argon gas in a real MPT geometry is simulated by a self-consistent two-dimensional axisymmetric model developed using the PIC–MCC method. Our model considers thermionic electron emission taking account of the Schottky effect, non-uniform argon gas density in the microdischarge passage and the secondary electron emission due to cathode bombardment by the plasma ions. Our model contains simplifications compared to some of the more sophisticated fluid models: it neglects the gas temperature distribution in the microdischarge cavity and considers only neutral particles as the background gas. However, our model can capture fundamental plasma physics that cannot be simulated with fluid models, such as non-local plasma kinetics and non-Maxwellian effects [26]. Because, unlike in fluid models, a Maxwellian energy distribution is not assumed, the temporal evolution of the energy distribution function for electrons and ions can be described in detail using the PIC–MCC method.

The article is organized as follows. Section 2 describes the numerical model and the simulation procedures. Particular attention is paid to the methods used to treat the collisions between species. Further, the approaches used to determine the characteristics of cathode surface sputtering by ion bombardment and the transport of sputtered atoms in the background gas are described in detail. The geometry and operating parameters used in the simulation is given as well. The calculated results for a typical base case are given in Section 3, and the effects of different discharge conditions are compared and discussed in Section 4. The conclusions of the work are summarized in Section 5.

2. Numerical Model

2.1 Basic assumptions

To investigate the characteristics of the microhollow discharge, a two-dimensional MCC-PIC numerical model was developed assuming the following conditions.

(1) The only species whose properties are calculated in the model are singly-ionized argon ions and electrons.

(2) The temperature of neutral particles is spatially uniform throughout the simulation, with a Maxwellian velocity distribution at a gas temperature of 1500 K used a typical discharge condition based on fluid model results obtained under similar conditions [20].

(3) The reactions taken into account are elastic, excitation, and ionization collisions for electrons, and elastic and charge-exchange collisions for ions:.

Elastic scattering, e + Ar→e + Ar

Electronic excitation, e + Ar→e + Ar*

Electron impact ionization, e + Ar→e + Ar^+ + e

Elastic scattering, Ar^+ + Ar→Ar^++ Ar

Charge transfer, Ar^++ Ar→Ar + Ar^+

The motion of excited-state atoms is not considered, and the Coulomb interactions between charged species are not taken into account due to the low ionization degree in current simulation.

(4) The coordinate system is axisymmetric; a given number of particles or superparticles representing ions and electrons, with axial and radial velocity components, are loaded in a two-dimensional mesh.

2.2 Calculation procedure

Each computational cycle with time step dt consists of the following steps:

(1) Electron emission from the surfaces of the cathode is described by the Richardson–Dushman equation, taking the Schottky effect into account [32]:

$$J(x) = DT^2 \exp\left(\frac{-e\varphi_0}{kT}\right) \cdot \exp\left(\frac{e}{kT}\sqrt{\frac{eE_C(x)}{4\pi\varepsilon_0}}\right) \tag{1}$$

Here ε_0 is the vacuum permittivity, $D = 2.6 \times 10^6 A \cdot m^{-2} \cdot K^{-2}$ is a constant that depends on the cathode material, $\varphi_0 = 2.0$ eV is the work function of the cathode material [33], T is the temperature of the cathode, with the same value as the gas temperature, and $E_C(x)$ is the electric field at the cathode surface, calculated by the Poisson solver in the PIC model. The initial energy of the emitted electrons follows a Maxwellian distribution at a background temperature.

(2) The potential distribution is calculated by the Poisson solver, and the particle acceleration in the electric field is then calculated. The self-consistent fields are used to change the particle velocities, and simulate the propagation of the electrons and ions to new positions in the thruster.

(3) The number and energy density of those ions reaching the cathode is recorded. The ions reaching the cathode surface play an important role in the secondary emission of electrons.

(4) The particles reaching the anode and cathode and the boundaries of the calculation area are removed. The secondary electron emission (SEE) is calculated when ions reach the surfaces of dielectric and the cathode. The coefficient of secondary electron emission on the surface of cathode, taken from the literature [34]-[35], is 0.07, and is defined as 0.01 on the surface of the dielectric.

(5) The cathode sputtering effect is calculated when ions reach the surface of the cathode, using the method presented in section 2.3.

(6) The electron–neutral (e-n) and ion–neutral (i-n) collisions are calculated, using the methods presented in section 2.4.

(7) The calculation then returns to step #1

2.3 Model of sputtering effect

If an energetic ion collides with a target surface, atoms will be ejected from the surface. This process is called sputtering. Only those ions whose energy are higher than the energy threshold of the cathode can cause sputtering [36]. Sputtering yield data are important for thruster design and lifetime prediction.

Sputtering is quantified by the sputtering yield, which is determined as follows [36]-[37]

$$Y(E)=\frac{3.56}{E_B}\frac{Z_1Z_2}{\left(Z_1^{2/3}+Z_2^{2/3}\right)^{1/2}}\frac{M_1}{M_1+M_2}\alpha s_n(\varepsilon)\left[1-\left(\frac{E_{th}}{E}\right)^{2/3}\right]\left(1-\frac{E_{th}}{E}\right)^{1/2} \tag{2}$$

Here, E_B is the binding energy of the cathode material, and the parameters Z_1, Z_2, M_1, M_2 are the atomic number and atomic mass of the incident ions (denoted by subscript 1) and the cathode material (denoted by subscript 2). The parameter α is a function of the target-to-ion mass ratio and can be approximated as

$$\alpha=\begin{cases}0.3\left(\frac{M_2}{M_1}\right)^{2/3}\left(K\frac{M_2}{M_1}+1\right)^{-1} & 0.5<\frac{M_2}{M_1}<10\\ 0.2\left(K\frac{M_2}{M_1}+1\right)^{-1} & \frac{M_2}{M_1}<0.5\end{cases} \tag{3}$$

Here the mean value of K is 0.4. The reduced energy, ε is given by

$$\varepsilon=0.0325\frac{M_2}{M_2+M_1}\frac{E}{Z_1Z_2\left(Z_1^{2/3}+Z_2^{2/3}\right)^{1/2}} \tag{4}$$

The reduced elastic cross section can be calculated with the analytical expression

$$s_n(\varepsilon)=\frac{3.441\sqrt{\varepsilon}\ln\left(\varepsilon+2.718\right)}{1+6.355\sqrt{\varepsilon}+\varepsilon\left(6.882\sqrt{\varepsilon}-1.708\right)} \tag{5}$$

E_{th} is the threshold energy of cathode material; sputtering will not occur unless $E>E_{th}$, which is given by

$$E_{th}=\begin{cases}E_B/\gamma(1-\gamma) & M_1\le 0.3M_2\\ 8E_B\left(M_1/M_2\right)^{0.4} & M_1>0.3M_2\end{cases} \tag{6}$$

$$\gamma=\frac{4M_1M_2}{\left(M_1+M_2\right)^2} \tag{7}$$

The atoms sputtered from cathode have an initial energy E_0 and angle θ, given by

$$E_0=\frac{E_B(r+\sqrt{r})}{1-r} \tag{8}$$

$$\theta=\frac{1}{2\arccos\left(1-2r\right)} \tag{9}$$

Here r is a random number between 0 and 1.

2.4 Treatment of collision processes

A. Electron–neutral collisions

We apply a null-collision method to treat the collisions between the electrons and the neutrals, which include both elastic collisions and inelastic interactions [38]. The energy of the particles remains unchanged in elastic collisions, but is altered in inelastic collisions. According to the null-collision method, when the collision probability is calculated, the neutrals, as the background species whose density can be described as a function of time and space, are assumed immovable. The charged species, on the other hand, are characterized by superparticles whose distribution functions evolve temporally and spatially as the superparticles move in the system in response to the local electric field.

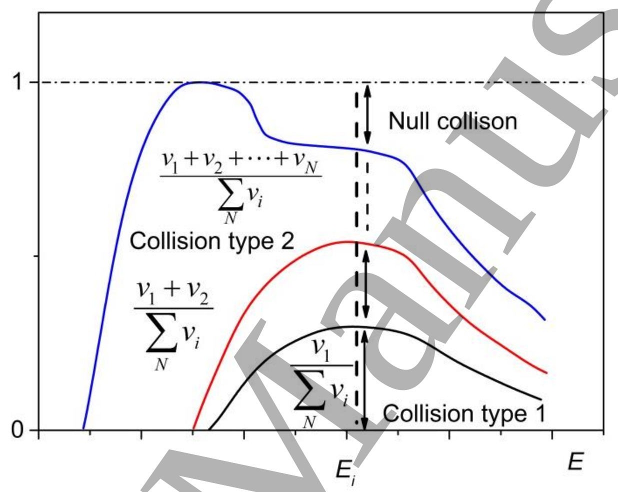

Fig.1 The addition of the null collision process results in a constant collision frequency over all energies. Here, the v_i are the frequencies of elastic scattering, excitation and ionization collisions.

According to the null-collision method (see Fig. 1), during each time step Δt, the largest number of the N_e electrons colliding with neutrals is calculated by the maximum collision frequency and gas density using

$$N_{coll} = N_e P_{coll} = N_e \left[1 - \exp(-\upsilon_{max} \Delta t)\right] \quad (10)$$

where the parameter υ_{max} is the maximum collision frequency and P_{coll} is the collision probability. When the values of probability P_{coll} are calculated, a set of random numbers between 0 and 1 is generated and compared with P_{coll}. If P_{coll} exceeds the random number, a collision occurs.

The maximum collision frequency, which corresponds to the maximum value of the sum of collision cross sections (see Fig. 1), is defined as a constant with value

$$\upsilon_{\max} = \max\left[n_t(x)\right] \max\left[\sigma_T(\varepsilon)\cdot\left(2\varepsilon / m_p\right)^{1/2}\right] \quad (11)$$

where $\max\left[n_t(x)\right]$ is the maximum neutral gas density, ε is the impact electron energy and $\sigma_T(\varepsilon)$ is the corresponding cross section. Since the maximum value of $\sigma_T(\varepsilon)\cdot\left(2\varepsilon / m_p\right)^{1/2}$ can be calculated for the full range of ε considered, the value of $\upsilon_{\max}$ is given before the calculation. Usually N_{coll} is much smaller than N_e, so this calculation method can save a lot of time.

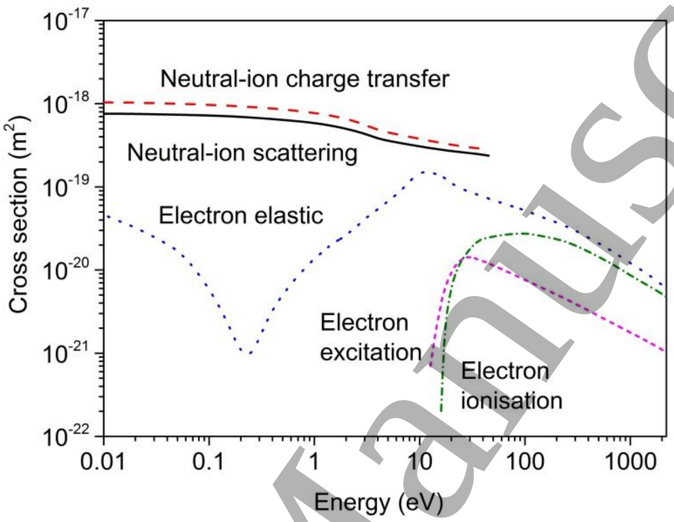

Fig.2 The set of collision cross-sections used.

Elastic scattering, excitation, ionization, and null collisions (i.e., the collisions which do not lead to a change in the energy or momentum of electrons) have been considered in the model; their cross sections as a function of electron energy [39] can be found in Fig. 2. A random number between 0 and 1 is generated to define the type of collision by comparing with the collision cross sections, which are normalized following the method described in Ref. [28] and are shown in Fig. 1. For the elastic scattering between the electrons and the neutral gas, the scattering angle χ is defined as

$$\cos\chi = 1 - \frac{2R}{1 + 8\varepsilon_r(1-R)} \quad (12)$$

where R is defined as a random number between 0 and 1, and ε_r is the relative energy of electron. When the energy of the electrons does not exceed 1 keV, equation (12) can be reduced to $\cos\chi = 1 - 2R$ using the isotropic hypothesis. The energy loss of the electrons in a scattering collision is $\Delta\varepsilon = \frac{2m_e}{m_n}(1-\cos\chi)$, where m_e and m_n are respectively the mass of an electron and a neutral.

Usually the velocity of neutrals and the mass of electrons can be ignored, so $m_n + m_e \approx m_n$ and the relative velocity $g \approx v_e$, the electron velocity. So the change of the neutral velocity can be ignored in the calculation of the electron–neutral collisions. For elastic scattering, the angles between the direction of the electron and the axis before and after the collision, θ_1 and θ_2 respectively, have the following relationship:

$$\cos\theta_2 = \cos\theta_1 \cos\chi + \sin\theta_1 \sin\chi \cos\phi \tag{13}$$

Here ϕ is the azimuth of electron; its value is a random number between 0 and 2π, and the new velocity of electron can be calculated from the new energy and direction.

When excitation or ionization occurs, the electron velocity is replaced by an equivalent velocity $\tilde{v}$, which is defined as $\tilde{v} = v\sqrt{1 - E_{th}/E}$ for excitation and $\tilde{v} = v\sqrt{1 - (E_{ej} + E_{th})/E}$ for ionization; here E_{th} is the threshold energy for excitation and ionization collisions, and E_{ej} is the energy of the ionization electron and is defined as

$$E_{ej} = R(E - E_{th}). \tag{14}$$

The velocity of the ion produced by electron impact ionization is chosen randomly from the Maxwell distribution corresponding to the gas temperature.

B. Ion–neutral collisions

Ion–neutral collisions are taken into account because the velocities of neutrals become non-negligible compared to the ion velocities for the gas temperatures produced. Two types of ion–neutral interactions are considered:

Elastic Scattering: $Ar^+ + Ar \rightarrow Ar^+ + Ar$

Charge-exchange collisions: $Ar^+ + Ar \rightarrow Ar + Ar^+$

The cross-sections of both types of collision are a function of the incident energy of the ion [40].

Elastic collisions can be expressed as

$$A^+(v_A) + B(v_B) \rightarrow A^+(v'_A) + B(v'_B) \tag{15}$$

The velocity after an elastic collision is defined by the hard-sphere collision model [41] and the isotropic scattering model is assumed to determine the scattering angle.

$$v'_A = \frac{1}{m_A + m_B}(m_A v_A + m_B v_B + m_B |v_A - v_B| R)$$

$$v'_B = \frac{1}{m_A + m_B}(m_A v_A + m_B v_B - m_B |v_A - v_B| R) \tag{16}$$

Here m_A and m_B are respectively the mass of the ion and neutral, and R is a unit vector in a random direction.

For charge-exchange collisions, the velocity of the ion and the neutral is exchanged after the collision. For a detailed description of the model used for calculation of ion–neutral collisions, see Ref. 28.

C. Neutral–neutral collisions

The neutral–neutral collisions that are considered are those between the sputtered atoms and the background gas neutrals; only elastic collisions are taken into account. A random number between zero and one is generated to compare with the collision probability between the sputtered atoms and background argon atoms, which is determined as follows.

$$P_{coll} = 1 - \exp\left[-n\sigma_{el}(E)\Delta s\right] \tag{17}$$

where n is the number density of the background gas and Δs is the distance moved during the time step. The cross section between neutrals $\sigma_{el}(E)$ is calculated as a function of collision energy from [42]:

$$\sigma_{el}(E) = nC\gamma^{-1/n}E^{-2/n} \tag{18}$$

where:

$$C = \frac{22.36\pi a_s^2}{2}\left(\frac{m_1}{m_2}\right)^{1/n}\left(\frac{2z_1z_2e^2}{a_s}\right)^{2/n} \tag{19}$$

$$n = 1 + 4\exp(-1.9\varepsilon^{0.1}) \tag{20}$$

$$a_s = 0.468\times10^{-10}/\left(\sqrt{z_1}+\sqrt{z_2}\right)^{0.667} \tag{21}$$

$$\varepsilon = \frac{m_2 E}{m_1 + m_2}\frac{a_s}{z_1 z_2 e^2} \tag{22}$$

$$\gamma = \frac{4m_1m_2}{\left(m_1 + m_2\right)^2} \tag{23}$$

Here Z_1, Z_2, M_1, M_2 are the atomic numbers and atomic masses of the incident neutral and target neutral; e is the electron charge.

The velocity after an elastic collision is defined by the hard-sphere collision model, and is given by (16).

2.5 Geometric model and operating parameters

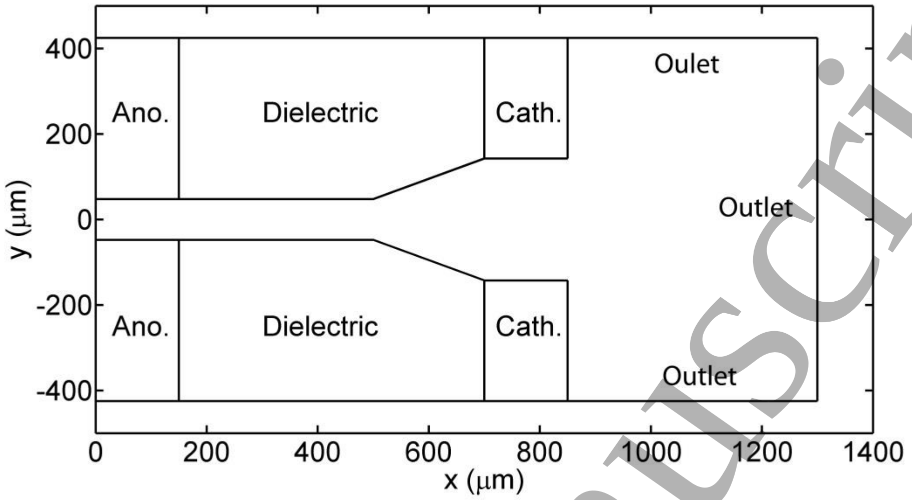

Fig.3 The geometry of the MPT device

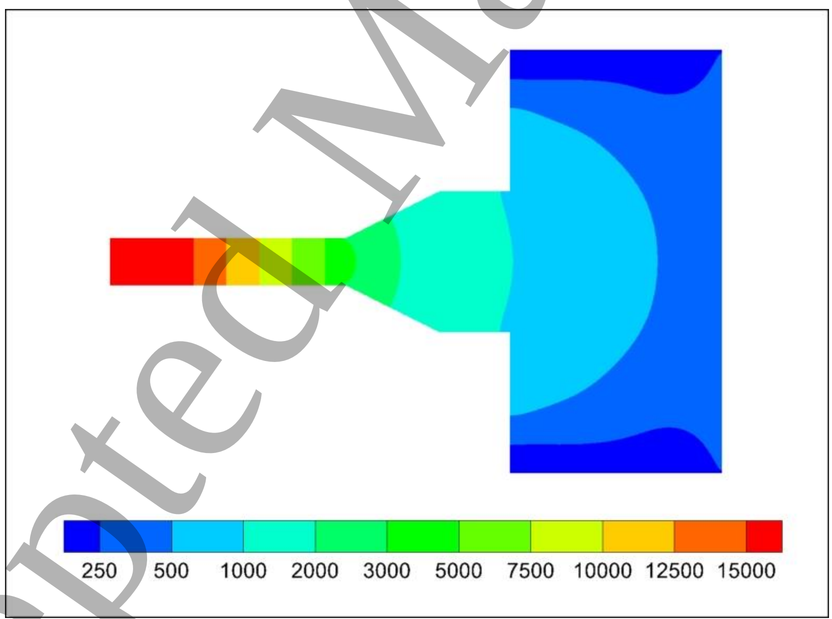

Fig.4 Background gas pressure distribution (unit: Pa)

Fig. 3 shows the geometry of the MPT device studied; the same geometry has been used in previous fluid model [20]. The geometry consists of an axisymmetric constant radius "pipe" section of 500 μm length, followed by a diverging section that is 200 μm in length, which is terminated by a 150 μm long constant radius section. The internal diameter of the cathode passage is 300 μm and the diameter of computation area is 850 μm. The anode and cathode are both 150 μm thick. The electrodes and the dielectric are made of aluminium and aluminium oxide respectively, which are typical materials used in MHCD thrusters [43].

The neutral species are treated as the background gas with a steady density distribution which is calculated by solving the Navier–Stokes equations [44]. The distribution of neutral argon species is used as input in the subsequent calculations of the discharge. The flow direction is from the left inlet at x = 0 μm (upstream) to the right exit of the thruster at x = 850 μm (downstream) in Fig. 3 and the background pressure distribution is showed in Fig.4. The flow enters a pipe section with a constant radius on the left and leaves out of the domain on the right. For the base case, the pressure at the inlet is given as 150 Torr and the outlet boundary out of the thruster (see indicated in Fig.3) is set 1.0 Torr. We use a constant anode voltage of 750 V and the temperature of the cathode is set equal to that of the background gas at a constant 1500 K. As noted in section 2.2, the work function of the cathodes is set to 2.0 eV; this is based on measurements [33]. It is noted that there exist large differences in the work function of aluminium oxide, due to the different manufacturing methods of the aluminium oxide films. The influence of operating parameters such as work functions, the discharge voltage and the discharge pressures on discharge behaviour is discussed later.

In the simulation, the total number of simulated particles was varied in the range of 10^5 to 10^6; this was limited by the available computational resources. The grid size varies as the radius changes; *dx* and *dy* are varied in the range from 10^{-5} to 10^{-6} m and *dy* has smaller values near the wall. The time step is mainly controlled by the requirement to have <10% of collisions each time step, since the Courant condition [45] $dx/V_{max}<dt$ is satisfied under the given conditions. Here, V_{max} is the largest electron velocity obtained at given condition $V_{max} = \sqrt{2e\varphi/m_e^2}$ where e, φ and m_e are the electron charge, the applied electric potential and the electron mass. Following this principle, we gives a typical time step dt =1.0×10^{-13} s for electrons. Indeed, in our current work, this parameter is varied according to the computational requirements. For example, if the gas pressure increases, the time step is needed to be further decreased. Also, the convergence analysis showed that an increase in φ requires a decrease in the space step.

3 Results and discussion

3.1 Breakdown phase

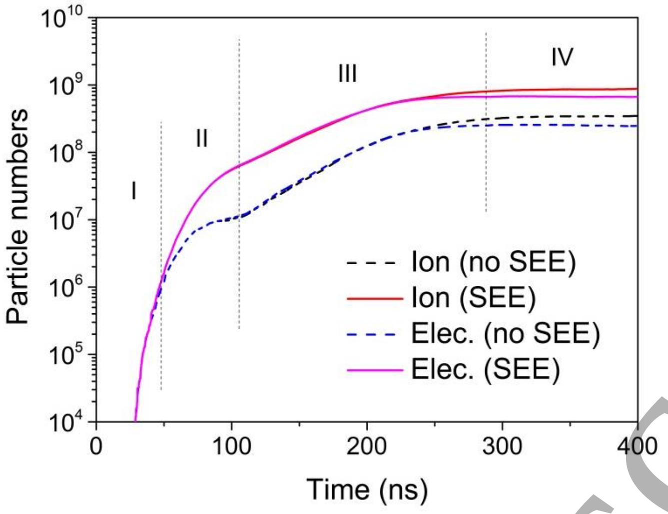

Fig.5 Time evolution of total number of electrons and ions in the computational domain

Fig. 5 shows the time evolution of total numbers of electrons and ions for the base case, including and neglecting the effect of SEE. As we can see, the whole discharge progress can be divided into 4 stages. The first three stages are related to the breakdown phase and the last stage is a steady-state phase. It is found that considering SEE increases the total number of charged particles in the latter 3 stages. This is because the secondary electrons emitted from the cathode surface by ion bombardment participate in the discharge processes and enhance the electron impact ionization rate, increasing the concentration of both electrons and argon ions.

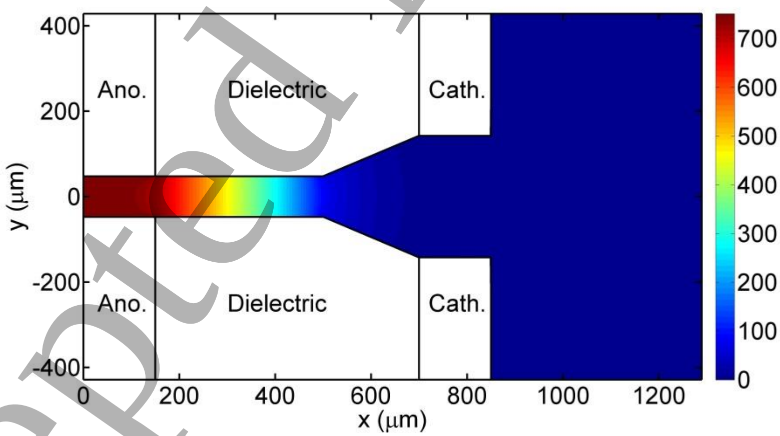

(a)

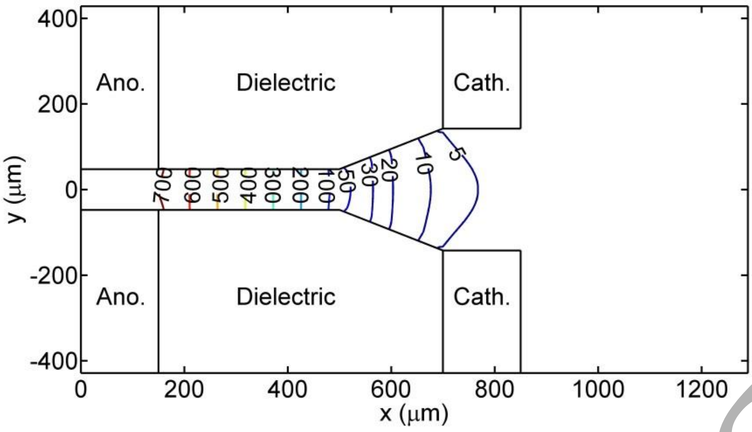

(b)

Fig.6 (a) Two-dimensional distribution and (b) contour map of electric potential (in V) at *t* = 0 ns.

In the initial stage, before *t* = 50 ns, as indicated by stage I in figure 5, electrons emitted from the cathode are accelerated under the driving force of the electric field. However, electron impact ionization, which has a high threshold energy level of 15.8 eV, cannot occur until the electrons gain sufficiently energy from the electric field. Therefore, the initial electric potential distribution at *t* = 0 ns, shown in Fig. 6, hardly changes because the electron and ion densities are still too low to modify the electric field. This period corresponds to the first stage of breakdown, in which only a small number of thermionically-emitted electrons exist in the thruster and almost no reactions occurs in the calculation volume. It is concluded that the contribution of the bulk electrons, created by gas ionization, to the total electron population is still very small compared to the emitted electrons in this stage.

Fig.7 Two-dimensional distribution of (a) electron number density, (b) ion number density and (c) electric potential, and (d) contour map of the potential distribution, at *t* = 80 ns. A logarithmic scale is used for the species number densities (unit: m^{-3}), and the electric potential is in V.

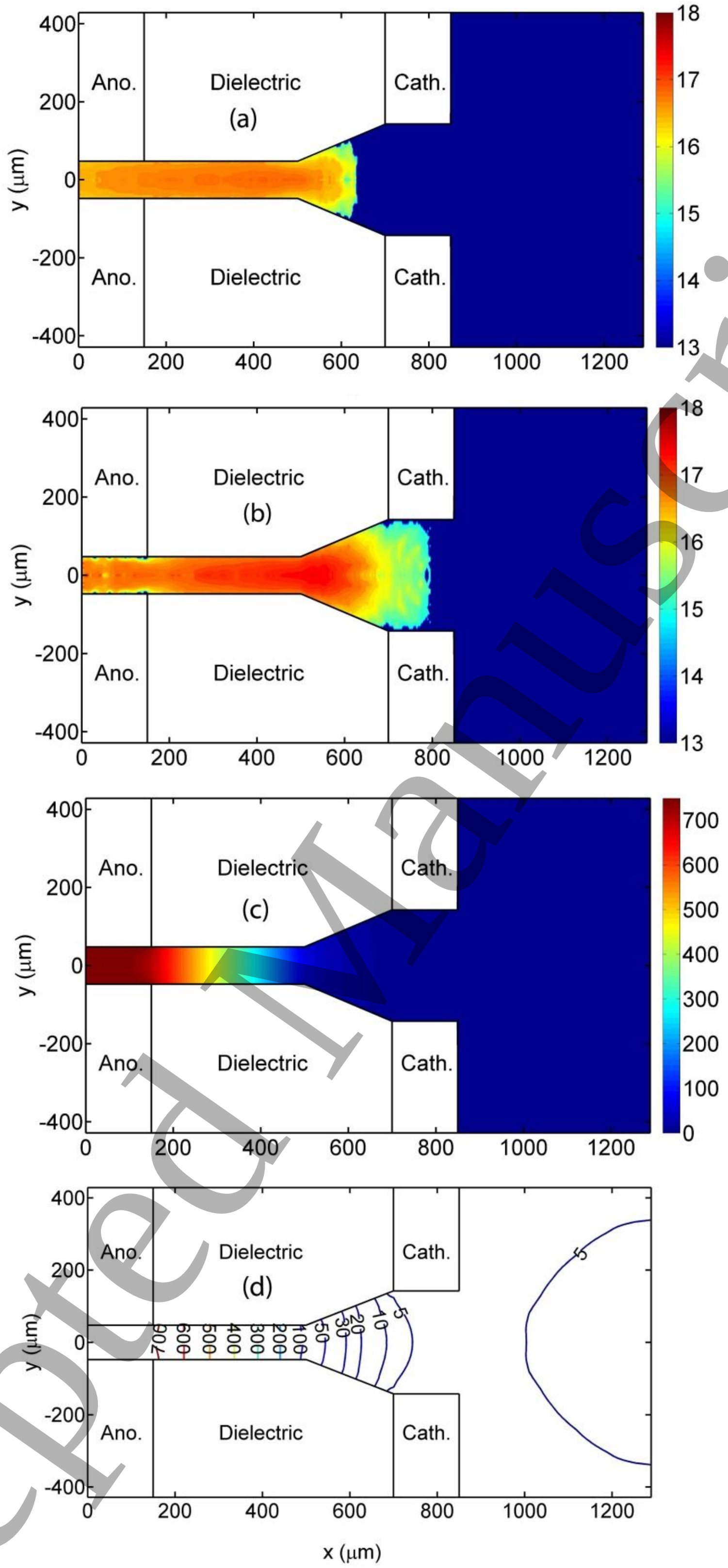

Fig. 7 shows the typical discharge properties in the second stage of the breakdown phase, from 50 ns to 100 ns. The potential inside the hollow passage starts to become slightly altered as the density of the ions and electrons increases. After t = 50 ns, the electron energy, which increases due to the acceleration by the applied electric field between the electrodes, exceeds the ionization threshold level of argon atoms (15.8 eV) and new electrons start to be created by electron impact ionization of the neutral particles. As the electrons drift much faster than ions because of their higher mobility, they propagate upstream more rapidly. This leads to an overpopulation of ions density, mainly in the expansion nozzle segment, and hence an increase of the local electric potential. During this stage, the electron number density is rapidly multiplied by the electron impact ionization in the core region of the discharge, $x = [500, 600]\,mm$. Newly-produced ions and electrons begin to move in opposite directions, driven by the electric field. The electrons mainly move in the negative x-direction while the ions acquire significant velocities downstream. At this stage, almost no discharge occurs near the cathode because electron impact ionization in this region is weak as a result of the low energy of thermally-emitted electrons (0.1098 eV). In the core region of discharge, the number density of positive ions reaches around 2.5 x 10^{17} m^{-3}. The number density of electrons is only around half that of the ions because of the higher electron drift velocity discussed above. As shown in Fig. 7(b), the number density of ions is around 1.0 x 10^{17} m^{-3} in the region, which is higher than that of electrons, indicating that the discharge propagates towards upstream. If we compare the electric fields shown in Fig. 6(b) and 7(d), we see that electric field is not significantly altered by the discharge. We also find that secondary electron emission has a negligible influence in this stage, due to the very small number density of electrons.

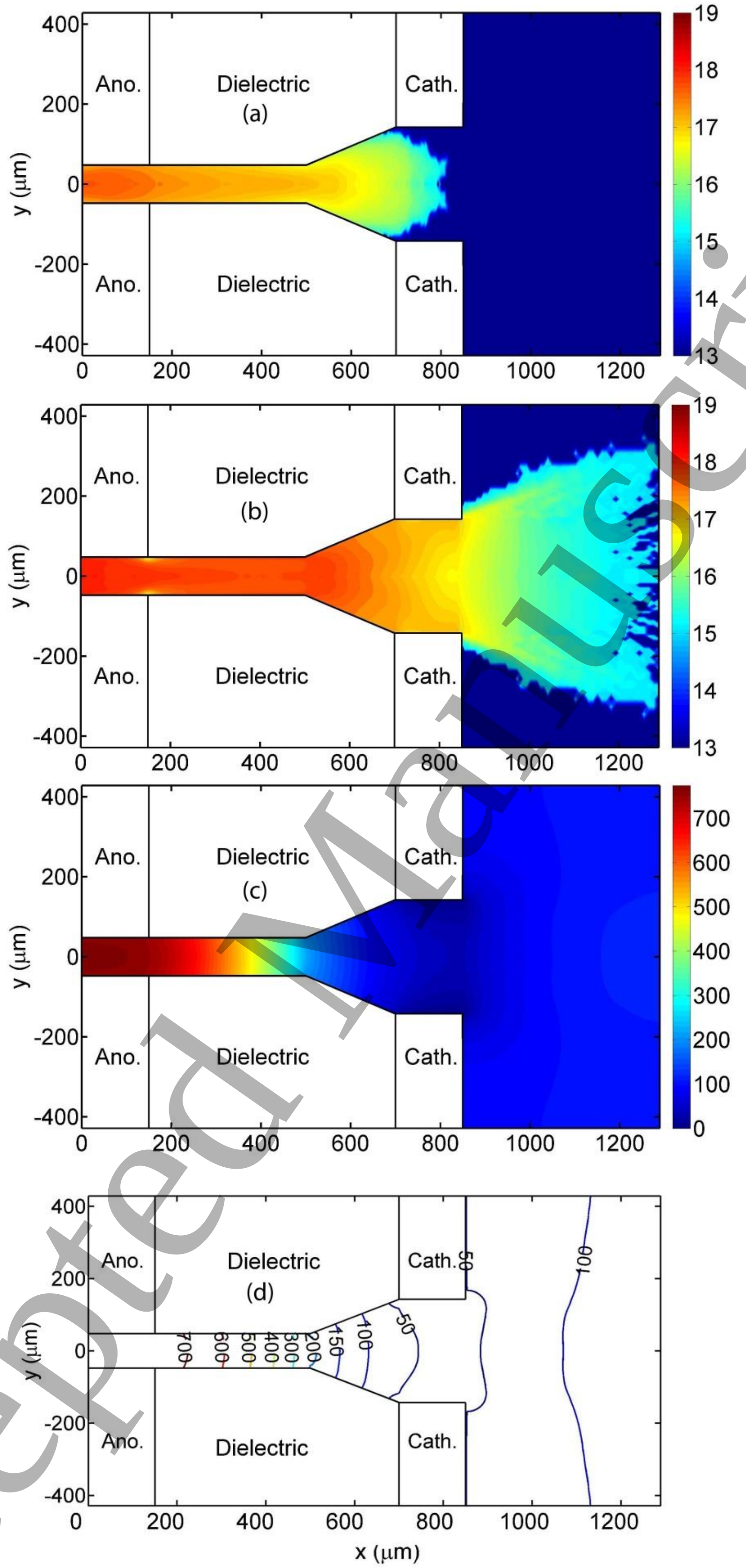

Fig.8 Two-dimensional distribution of (a) electron number density, (b) ion number density and (c) electric potential, and (d) contour map of the potential distribution, at t = 180 ns. A logarithmic scale is used for the species number densities (unit: m^{-3}), and the electric potential is in V.

Figure 8 shows the results during the third stage of the discharge, which corresponds to times from 100 ns to 280 ns. During this stage, electrons that are accelerated by the electric field propagate towards the anode near the left-hand boundary of the thruster device, and react with neutral argon near the anode. The plasma density inside the hollow passage reaches around 1.0 x 10^{18} m^{-3}. Compared with the results for the second stage shown in Fig. 7, there is an additional reaction region that is apparent between $x = [0,150]$ μm, in which electrons acquire sufficient energy to ionize the neutral particles, increasing the plasma formation rate. It is noted that the density of ions is around 4.5 x10^{18} m^{-3} in this region, which is higher than that in the neighbouring regions. In the region $x = [500,600]$ μm, which was the core of the discharge in the second stage, there is still a local maximum value of the ion number density, around 3.0 x 10^{18} m^{-3}. In contrast, the number density of electrons gradually decreases in the downstream direction, from a value of 1.9×10^{18} m^{-3} at x = 50 μm to 0.9×10^{18} m^{-3} at x = 500 μm. The region $x = [500,600]$ μm, in which the highest density of electrons occurred in the first stage, no longer has even a local maximum density. In the third stage, the positive ions produced in the discharge cavity, which are accelerated downstream, gain a radial velocity component in the nozzle expansion segment as a result of the radial component of the applied electric field. Their trajectories deviate from the central axis toward the cathode surface, leading to a non-uniform radial density distribution. As indicated in Figs. 8(c) and 8(d), the accumulation of ions near the cathode surface leads to an increase in the local electric potential, which exhibits a shallow well-shaped distribution in the axial direction. The depth of this well exceeds the ionization threshold of argon, and the plasma produced by impact ionization processes becomes denser in the cathode region. The increased potential outside the thruster can be explained by the overpopulation of positive ions in this region, which results from their mobility being higher than that of electrons.

In this stage, as a result of the increased ions impact on the cathode surface, secondary electron emission begins to play a significant role in the discharge development. This can be seen from Fig. 5; if SEE is ignored, then the total plasma number density is underestimated by 5%, Fig. 8 (d) shows that the region for which the electric potential is above 700 V is enlarged from $x = [0,150]$ μm to $x = [0,250]$ μm; this is because the increased plasma density and electrical conductivity decreases the potential gradient here.

3.2 Steady-state phase

The simulations show that for the given parameters, steady-state operation of the MPT is reached around t = 280 ns, which is defined as the final stage of DC discharge development. In this stage, a dynamic equilibrium is reached between the production of charged particles and their disappearance by escaping from the calculation area. The total number of charged particles in the computational domain, 8.8 x 10^8 and 3.5 x 10^8 for ions and electrons respectively, does not vary with time, which is as indicated in Fig. 5. Because the mobility of the electrons is much larger than that of ions, the total number of ions in the computational domain is about twice that of electrons after steady state is reached. The potential and the current at the surface of cathode also do not change as a function of time. The total number of ions and electrons without taking into account the secondary emission of electrons reaches around 6.7 x 10^8 and 2.5 x 10^8 for ions and electrons respectively. This is 30% lower than obtained when taking this effect into account, indicating that the secondary emission of electrons has a strong influence on the discharge properties.

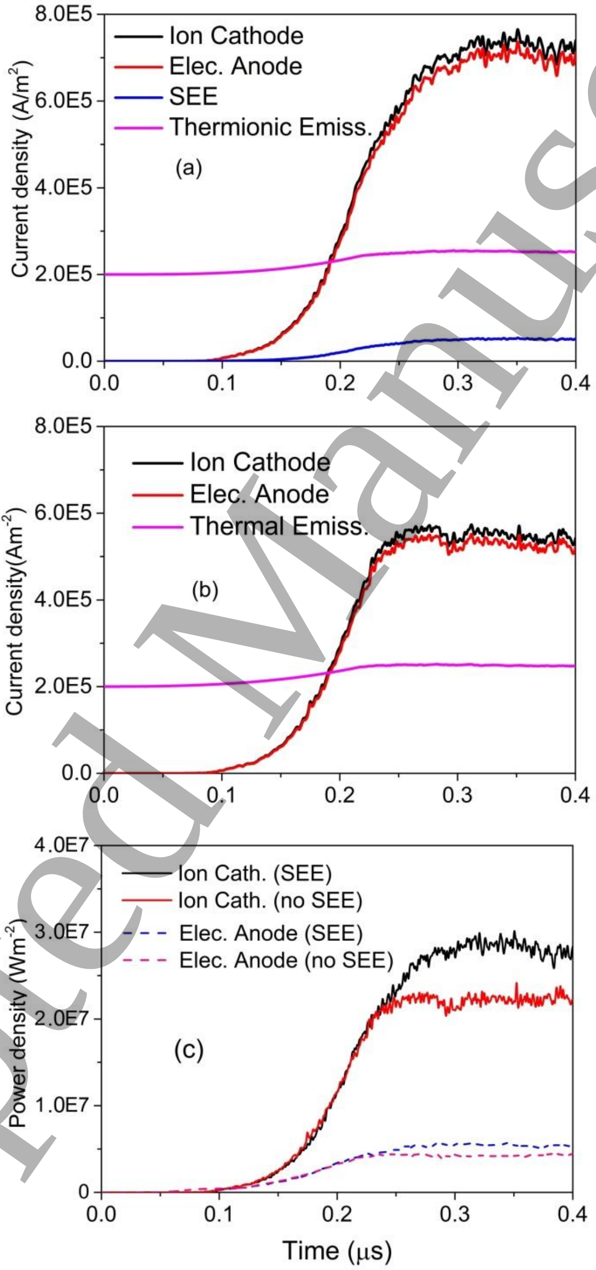

Fig.9 Discharge parameters over the full duration of the calculation. (a) Current density taking SEE into account (b) Current density without taking SEE into account (c) Power deposition density with and without taking SEE into account.

Fig. 9 shows the time evolution of the discharge current and power deposition density with and without taking SEE into account. It shows that taking SEE into account increases the current and power deposition density. The average current density once steady state is reached is 7.2 x 10^5 A/m^2 for ions at the cathode (black line in Fig. 9(a)) and 6.9 x 10^5 A/m^2 for electrons at the anode (red line in Fig. 9(a)) if SEE is taken into account. In contrast, if SEE is neglected, the values obtained are of 5.5 x 10^5 A/m^2 and 5.3 x 10^5 A/m^2 respectively for the ions at the cathode (black line in Fig. 9(b)) and the electrons at the anode (red line in Fig. 9(b)). We also find that the average current density carried by the thermionically-emitted electrons from the cathode surface does not change very much during the discharge, varying only from 2.0 x 10^5 A/m^2 to 2.5 x 10^5 A/m^2 (pink line in Fig. 9(a)). This is because the electric field at the cathode surface only increases slightly during the discharge, leading to a small increase of the current through the enhanced Schottky effect (see equation (1)). The SEE current density at the cathode (blue line in Fig. 9(a)) reaches 5.0 x 10^4 A/m^2 under steady-state conditions. This is only 20% of that carried by the emitted electrons at the cathode surface. However, this can affect the discharge current, as discussed above, as well as the power deposition density, as presented in Fig. 9(c).

With SEE taken into account, the average power deposition density at the cathode surface due to the ion bombardment reaches 2.8 x 10^7 W/m^2 (black line in Fig. 9(c)), which is much higher than the power density taken away by the thermionically-emitted electrons (3.1 x 10^4 W/m^2) and the secondary electrons (6.2 x 10^3 W/m^2), indicating that the power deposition by the ion influx is a dominant cathode heating mechanism. The power deposition density associated with the electron current at the anode surface is 5.6 x 10^6 W/m^2, which is much lower than that at the cathode surface due to the ion bombardment. This is explained by the fact that the electrons arriving at the anode have a lower average energy than the ions reaching the cathode surface. This is because once they are produced by electron impact ionization, the ions experience acceleration over a long distance before they arrive at the cathode.

Neglecting SEE reduces the average power deposition density from 2.8 x 10^7 W/m^2 to 2.2 x 10^7 W/m^2 at the cathode surface and from 5.6 x 10^6 W/m^2 to 4.3 x 10^6 W/m^2 at the anode surface, showing that SEE plays an important role in the discharge, even though the SEE current density is much smaller than that carried by the thermionically-emitted electrons. The latter also explains the significant difference between the total electron and ion numbers and current densities shown in Fig. 5. This trend is different from that found by Levko et al. [22] for an orificed micro-hollow cathode discharge. The insignificant difference between the total electron and ion numbers and current densities in their work can be explained by the lower work function of tungsten (1.5 eV) that they used, which produces a much higher current density of thermionically-emitted electrons than of secondary electrons. What's more, the geometric structure and calculate conditions between their works and ours are significantly different, and the background gas is xenon in their works compared to the argon in ours. These factors result in the differences in computational results.

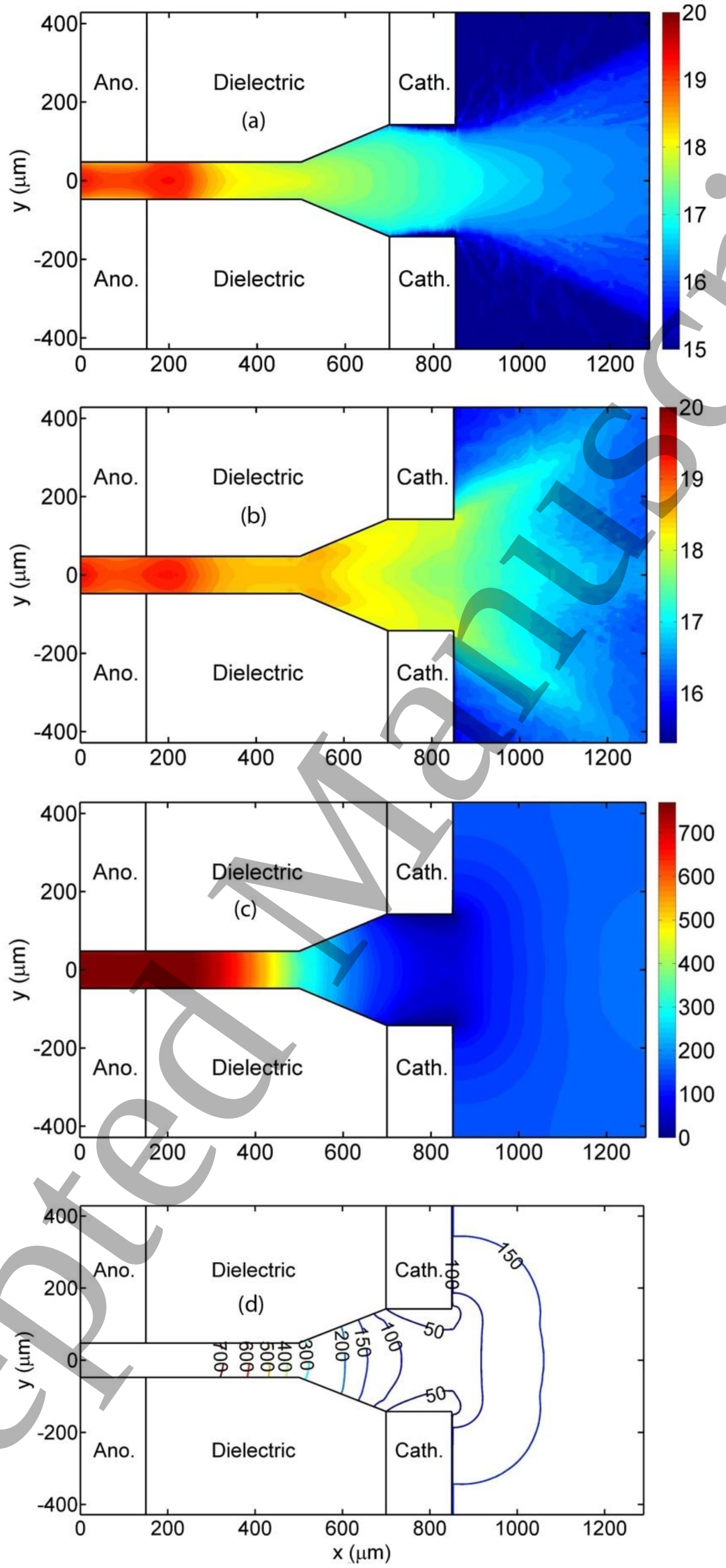

Fig.10 Two-dimensional distribution of (a) electron number density, (b) ion number density and (c) electric potential, and (d) contour map of the potential distribution, at t = 300 ns. A logarithmic scale is

used for the species number densities (unit: m^{-3}), and the electric potential is in V.

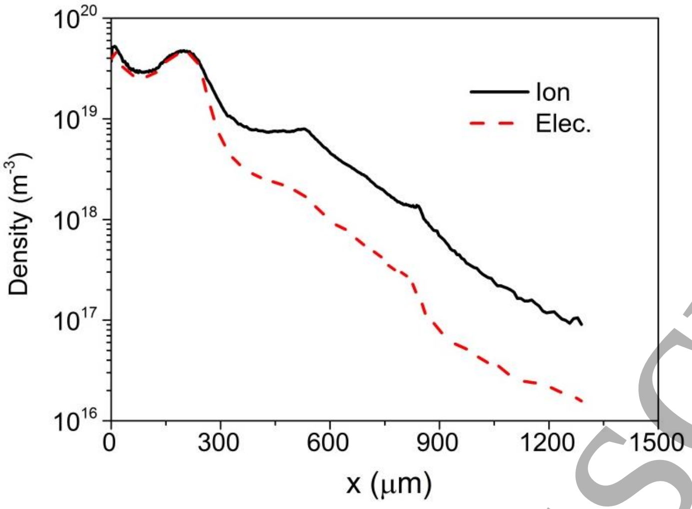

Fig 11 One-dimensional axial distribution of ions and electrons

Fig.10 shows the distributions of the electrons and ions number densities under the steady-state conditions. The one-dimensional distributions of the number densities along the central axis are also presented in Fig.11. The discharge core moves into the region $x = [0, 300]\ mm$, where quasi-neutrality prevails with a maximum number density of electrons and ions of around 2.1 x $10^{19}\ m^{-3}$. This indicates that bulk ionization is sustaining the discharge. In this region, the electrons that are propagating towards the anode under acceleration by the electric field interact with the background neutral species. These have the highest densities here because the pressure is highest, leading to an increasing collisional ionization frequency and enhanced bulk ionization. We also find that the electric field is quite weak in this area because of the high charged particle concentration and hence high electrical conductivity. Note that a slight drop of the charged particle density occurs near the location $x = 100\mu m$, due to the decreasing pressure and hence background neutral number density. In the region near the anode exit $x = [200, 300]\ mm$, the charged species number densities have a local maximum value. This is attributed to the electrons acquiring sufficiently energy in the region $x = [300, 700]\ mm$, where there exists a quite large electric field and the charged particles are quickly accelerated under the driving force of the electric field. In this acceleration region, the number density of ions is larger than that of electrons, which have greater mobility; this can lead to an increased electric potential and hence change its distribution, as indicated in Fig. 10. Additionally, in the region $x = [300, 700]\ mm$, the densities of ions and electrons decrease rapidly in the downstream direction from the position $x = 300\mu m$, due to the decreasing background pressure and hence neutral species number density. Our model finds that there exists a plasma plume in the region out of the thruster.

Available experimental images of optical emission from argon MHCDs confirm our prediction of significant discharge activity outside the cathode hollow region [17]. Moreover, the diameter of the discharge outside of the thruster itself is much larger than the hollow diameter itself. Experimental observation [17] as well as the fluid model [20] can also confirm this.

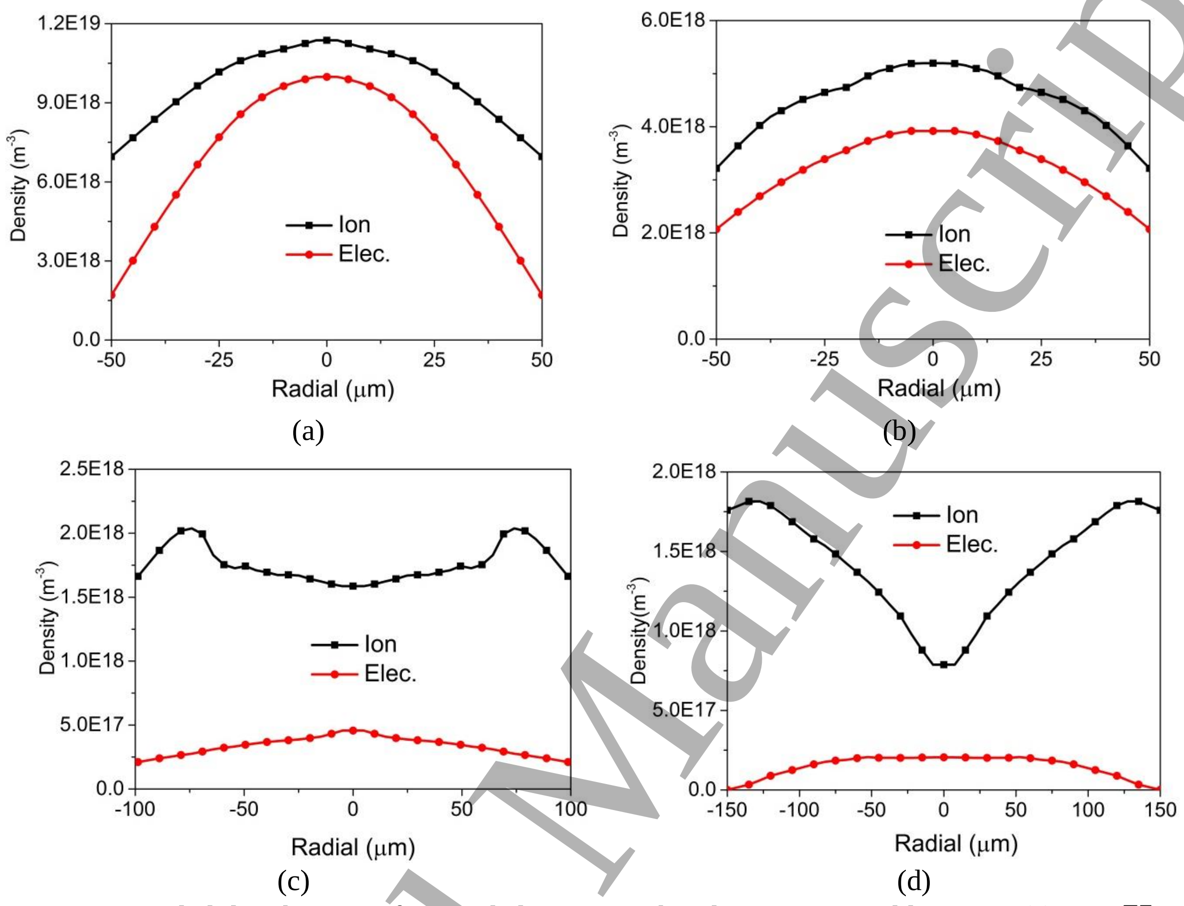

Fig.12 Radial distributions of ion and electron number densities at axial locations (a) $x = 75\mu m$, (b) $x = 400\mu m$, (c) $x = 600\mu m$, (d) $x = 800\mu m$, which respectively correspond to the centre of the anode, pipeline, expansion nozzle section and cathode.

Fig. 12 presents the radial distribution of ion and electron number densities at the centre of the anode, pipeline, expansion section and cathode. At the centre of the anode section, as shown in Fig. 12(a), the radial distributions of both the ion and electron number densities are characterized by maxima on the central axis, with rather rapid decreases away from the axis, showing the formation of plasma sheaths in the vicinity of the anode. The ion density is slightly larger than that of the electrons on axis. However, the difference increases towards the anode surface due to the sheath effect, under which a larger fraction of electrons than ions are absorbed by the anode. Fig. 12(b) shows the same general trend occurs in the pipeline; however, the densities of ions and electrons are respectively only 25% and 10% of those at the centre of anode. This can be explained by the decreasing pressure and hence neutral number density, which decreases the bulk ionization rate. Fig. 12(c) shows that, due to the expanding geometry in the expansion nozzle, the ions acquire a radial velocity component under the driving force of a radial electric field and begin to propagate towards the cathode surface. The ion density on axis is therefore smaller than near the cathode boundary. The slight reduction of the ion density near the surface of the dielectric material is mainly caused by the absorption of the ions by the material. The other factor that contributes to the reduction of the ion density on axis is the slight decrease of the pressure (see Fig. 4) and hence the neutral species density from the boundary towards the axis, which decreases the collision ionization frequency. Fig. 12(d) shows the same tendencies in the cathode region. The ion density on axis is smaller than that at boundary mainly because the ions generated in the upstream region are accelerated rapidly towards the cathode surface under the influence of the radial electric field.

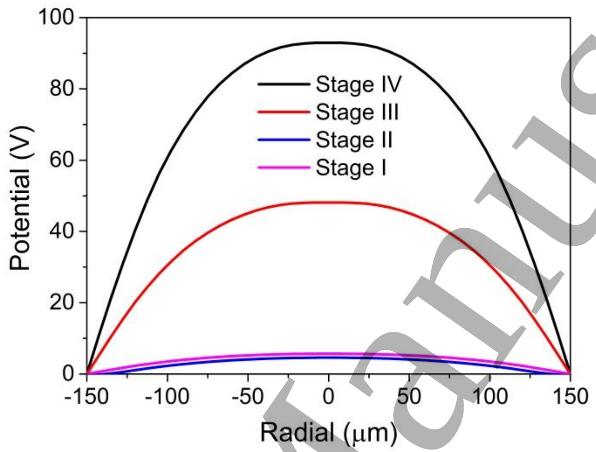

Fig.13 Radial distribution of electric potential at $x = 800\mu m$ for the different stages, at t = 50 ns, 80 ns, 200 ns and 300 ns

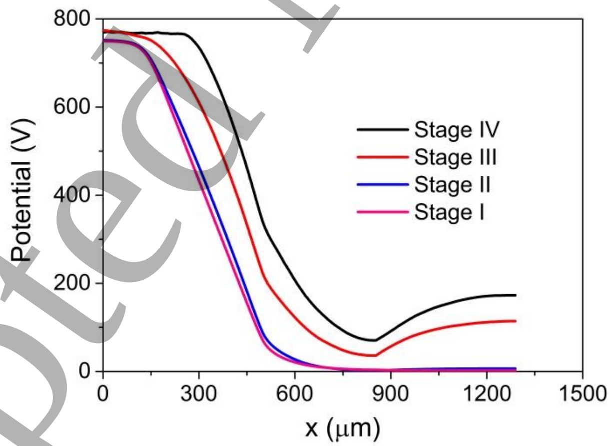

Fig.14 Axial distribution of electric potential along the central axis for the different stages, at t = 50 ns, 80 ns, 200 ns and 300 ns

The radial and axial distributions of electric potential at t = 50 ns, 80 ns, 200 ns and 300 ns, which respectively correspond to the four different discharge stages, are plotted in Figs. 13 and 14 respectively. They show that the electric potential distribution during the first stage has no apparent change compared to the initial state. In the second stage, the electric potential increases slightly along the axis because of the accumulation of ions, which are produced by bulk ionization in the discharge area. With the further increases of charged species in the thruster and the development of the discharge, both the radial electric potential at the centre of the cathode and the potential along the central axis increase until a steady-state condition is reached. The location $x = 800\mu m$, for which results are shown in Fig. 13, corresponds to the cathode centre; hence the electric potential drops to zero at the electrode with an extremely high gradient due to the influence of sheath. Within the cathode–anode gap, acceleration of ions occurs mainly in the layer formed between the plasma acquiring almost the anode potential at around $x = 300\mu m$ and the plasma in the centre of the cathode. Downstream from the cathode centre, the electric potential gradually increases along the central axis to around 200 V because of the overpopulation of ions. This forms a potential barrier of around 100 V and prevents the ions from propagating out of the discharge thruster. Further, the electric potential increases with the distance from the cathode surface towards the central axis. The potential difference increases as the discharge develops. Thus, some of the ions can acquire energy sufficiently high to cause significant sputtering of the cathode.

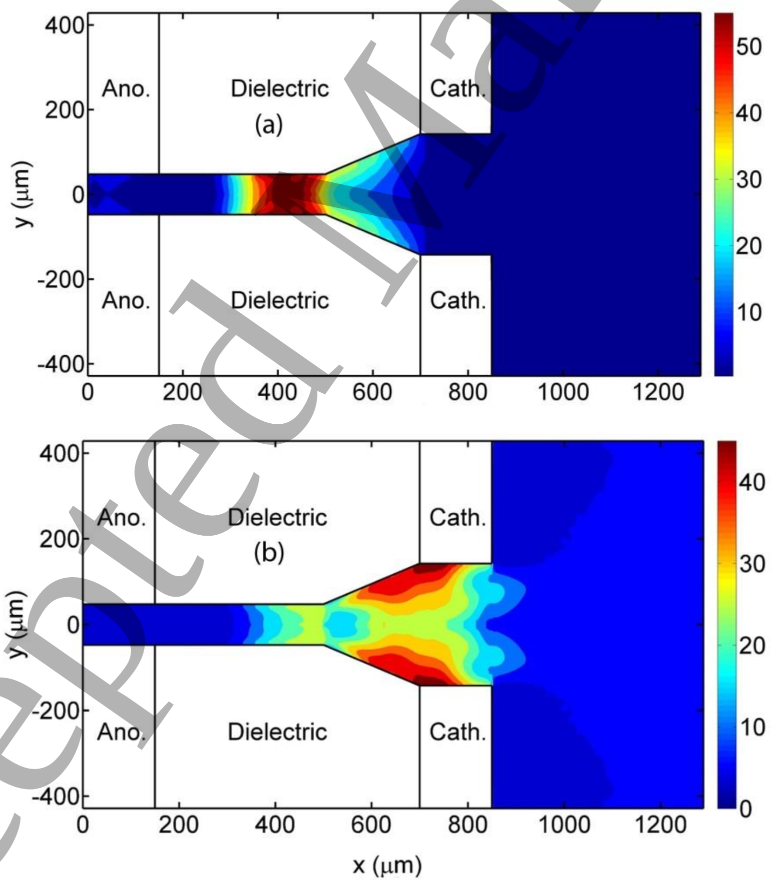

Fig.15 Average energy distributions of (a) electrons and (b) ions under steady-state conditions

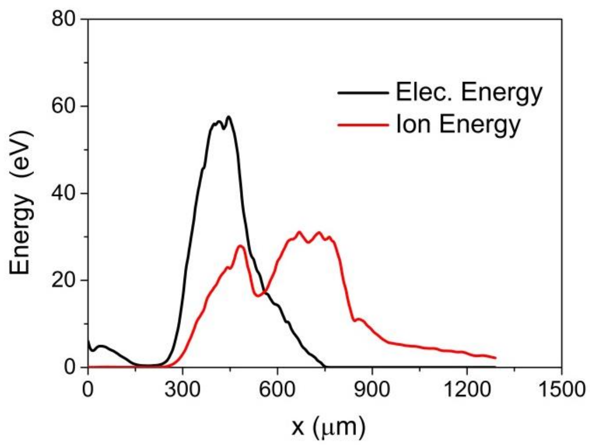

Fig.16 Axial distribution of average ion and electron energies

Fig. 15 presents the average energy distributions of electrons and ions under steady-state conditions. The axial distribution of the average energies of electrons and ions along the central axis is also presented in Fig. 16. Electrons emitted from the cathode are accelerated in the upstream direction by the electric field. In the region $x = [500, 600]\ mm$, electrons attain an average energy exceeding the ionization threshold and ionization reactions become important. In the region $x = [300, 500]\ mm$, there is a large potential gradient and hence a large electric field, which accelerates the electrons and increases the average electron energy to an extremely high value of around 58 eV. In the region $x = [0, 300]\ mm$, the average energy of electrons is greatly decreased. This is attributed to the very high impact ionization rate that occurs as a result of an increasing pressure and hence neutral species density in this region; a large fraction of the electron energy is consumed by bulk ionization.

In the region $x = [0, 500]\ mm$, moving downstream from the inlet, the average ion energy gradually increases to around 25 eV under the driving force of electric field. Then, in the region $x = [500, 600]\ mm$, a slight drop of the average ion energy to around 16.5 eV occurs. This is because the electrons emitted from the cathode reach the ionization threshold in this region, and the ions that are produced by impact ionization initially have a relatively low energy. In the region $x = [600, 800]\ mm$, the ions are accelerated towards the cathode surface by the electric field leading to a high average energy. In the region $x = [800, 1300]\ mm$, the ions are decelerated by a reverse electric field and hence their average energy decreases along the axis in the downstream direction.

Our predicted average electron energy is of tens of eV. This is consistent with the prediction by the fluid model using the same MPT geometry [46]. Moreover, the experimental studies of emission from highly excited states of ionic species in noble gas MHCD also provide indirect evidence for the high electron temperatures in these discharges [47].

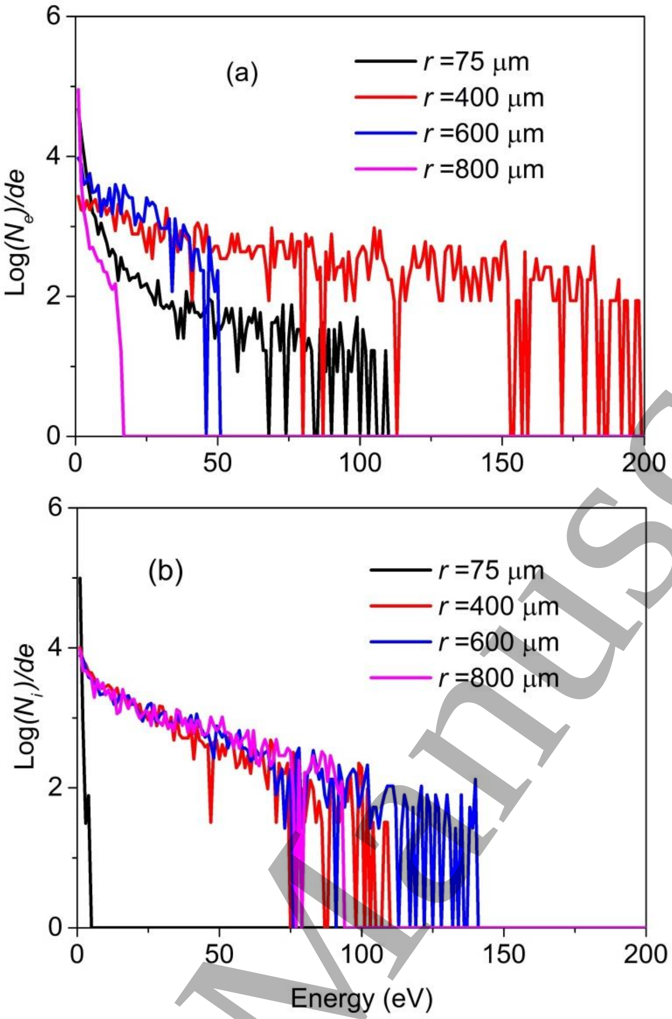

Fig.17 (a) Electron and (b) ion energy distribution functions on axis under steady-state conditions, at different axial positions.

Fig. 17 presents the electron and ion energy distribution functions under steady-state conditions obtained at different axial positions. At the location $x = 800\mu m$, which corresponds to the cathode centre, we can see the energetic electrons at the tail of energy distribution function acquire a maximum energy of around 16 eV. As they move upstream, the electrons are effectively accelerated by the electric field near the cathode because the mean free path of these electrons (around 112 μm with a local pressure of 10 Torr at $x = 800\mu m$) is comparable with the propagation distance and the collision frequency is very small. The energetic electrons at the tail of energy distribution function acquire maximum values of around 50 eV and 200 eV respectively at $x = 600\mu m$ and $x = 400\mu m$. This also corresponds to an increased average electron energy, as we can see in Fig. 16. With the increase of the average electron energy and the pressure in the upstream direction, collisional ionization becomes more frequent and this consumes the energy of the energetic electrons. Therefore, the electron energy distribution at $x = 75\mu m$ becomes narrower, and can be characterized by a mean electron energy of around 5 eV.

The ion energy distributions are mainly affected by the acceleration in the electric field and the ion–neutral collisions. At the location $x = 75\mu m$, ion–neutral elastic collisions, which are most frequent at that location because the neutral density is largest near the inlet, lead to a narrow ion energy distribution characterized by a maximum ion energy of around 5 eV. With propagation downstream, the ion energy distributions at $x = 400\mu m$ and $x = 600\mu m$ becomes broad. At $x = 800\mu m$, the energetic ions are collected and absorbed at the cathode surface, and a reduction of the average ion energy occurs. The simulation results indicate significant deviations of the electron energy distribution from a Maxwellian function.

3.3 Cathode sputtering and thermalization of sputtered atoms

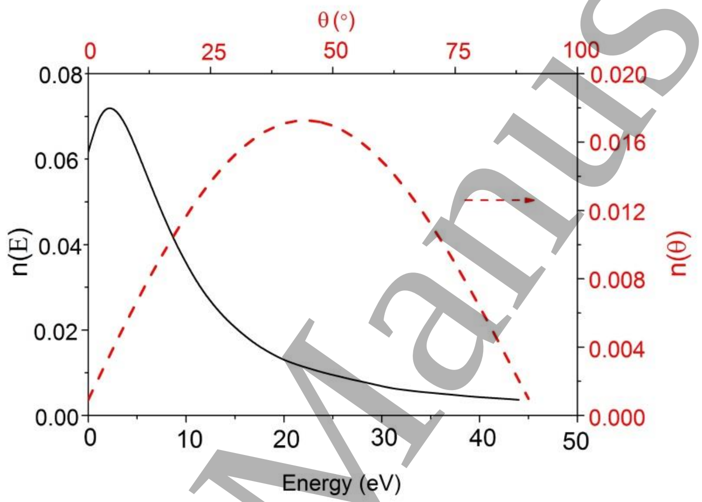

Fig.18 Initial energy and angular distributions of sputtered Al atoms at the centre of the cathode.

The ions accelerated by the electric field reach the cathode surface and produce sputtered Al atoms. The initial energy and angle distribution of sputtered Al atoms are shown in Fig. 18. We find that most sputtered Al atoms have energies lower than 15 eV and the scattering angle is largest around 45°.

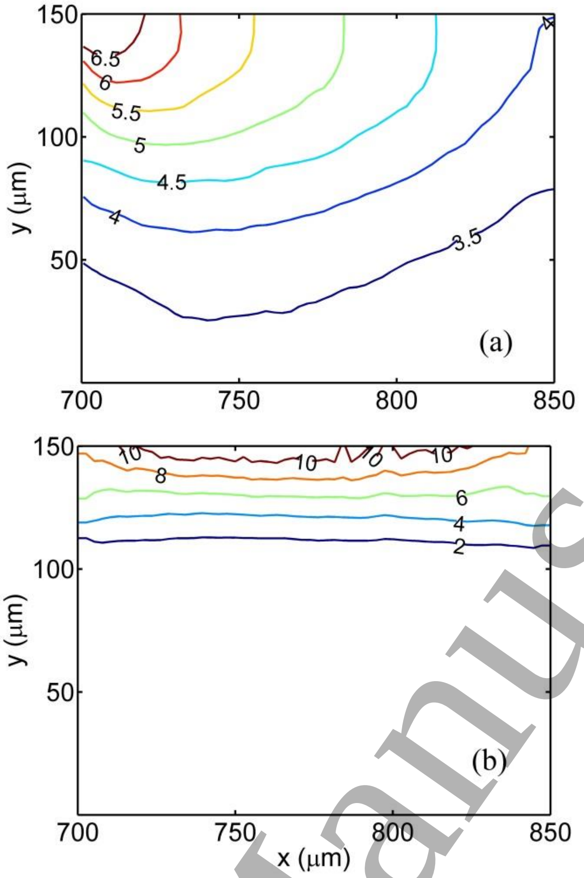

Fig. 19 Two-dimensional distribution of sputtered Al atoms near the cathode: (a) number density (unit: 1×10^{17} m^{-3}) (b) average energy (unit: eV)

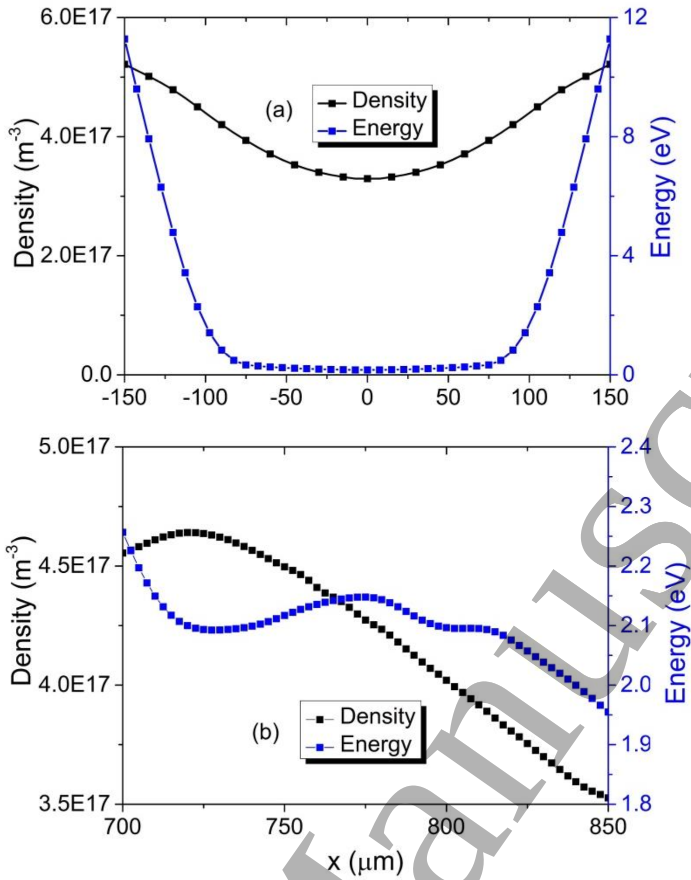

Fig.20 (a) Radial distribution at the centre of the cathode and (b) axial distribution at $y = 0\mu m$ of the number density and average energy of the sputtered Al atoms

Fig. 19 presents two-dimensional distributions of the number density and average energy of sputtered Al atoms near the cathode (at $x = [700,850]\mu m, y = [0,150]\mu m$). The axial and radial distributions of the sputtered Al atoms are also presented in Fig. 20. The number density and energy of sputtered atoms reach their maximum values, around 5.3 x 10^{17} m^{-3} and 11.28 eV respectively, at the surface of the cathode. The number density gradually decreases towards the central axis to the minimum value of 3.3 x 10^{17} m^{-3}. Similarly, their average energy also reduces rapidly to below 0.33 eV at a radial position of $75\mu m$ due to the energy exchange by elastic impact with the background species. Comparing this with the average translational energy of the background species, $5kT/2 = 0.3125eV$, we can conclude that most of the sputtered atoms have reached thermal equilibrium and are almost completely thermalized at the radial position of $75\mu m$.

We can see that the concentration of sputtered atoms decreases in the downstream direction. This can be explained by the decreasing ion number density and average energy, as shown respectively in Figs. 10(b) and 15(b). A higher concentration of ions and higher average energy generally lead to a higher incident power deposition density and hence a higher sputtering rate of the cathode material (see equation 2). The highest cathode erosion rate is $6.088 \times 10^{-13} mol/s$. Taking into account the mass density of the cathode material as well as the thruster diameter, this gives a value of $0.152 \mu m / h$. This is only 16% of that estimated for a larger orificed micro-hollow cathode thruster by Levko et al. [22], because of the differences of geometric structure, background gas and electrode parameters.

The initial energy of the sputtered Al atoms is determined randomly and is not affected by the energy of incident ions. Therefore, the energy of the sputtered Al atoms shows an almost uniform distribution along the axial direction. The slight reduction in the downstream direction is mainly a consequence of the more frequent collisional energy exchange between the sputtered Al atoms and the neutral argon atoms.

4 Influence of operating conditions

Table 1 Influence of work function, background temperature, inlet pressure and discharge voltage on the steady-state parameters of the micro-hollow cathode discharge.

Case	Work function	Inlet pressure	Voltage	Thermionic emission current density	Ion current density at the cathode	Electron current density at the anode	Ion power density at the cathode	Electron power density at the cathode	Secondary current density	Maximum ion number density
Unit	eV	Torr	V	A/m^2	A/m^2	A/m^2	A/m^2	W/m^2	A/m^2	m^{-3}
Base	2.0	150	750	2.52E+05	7.20E+05	6.90E+05	2.75E+07	5.58E+06	5.04E+04	2.10E+19
1	2.0	100	750	2.18E+05	1.75E+05	5.96E+05	3.33E+06	3.44E+07	1.22E+04	2.82E+18
2	2.0	200	750	3.00E+05	1.41E+06	3.09E+05	5.22E+07	1.45E+06	9.88E+04	6.54E+19
3	2.0	150	1000	2.55E+05	7.92E+05	7.30E+05	2.94E+07	7.33E+06	5.33E+04	2.25E+19
4	1.5	150	750	1.50E+06	3.43E+06	3.01E+06	1.85E+08	3.71E+07	2.40E+05	7.03E+19
5	4.0	150	750	0	2.71E+05	1.04E+06	6.40E+06	1.38E+07	1.90E+04	8.17E+18

In table 1 we present the results of additional simulations, which were carried out in order to examine the influence of the cathode work function, the inlet pressure, and the discharge voltage on the micro-hollow cathode discharge properties. We keep other parameters unchanged when changing one of these parameters. The dependence of seven properties, i.e. the thermionic emission current density, ion current density at the cathode, electron current density at the anode, ion power density at the cathode, electron power density at the cathode, secondary current density and maximum ion number density, on the parameters are presented.

1) Effect of background pressure

Decreasing the inlet pressure, as is done in case 1, leads to a decrease in the background pressure and hence the neutral species number density. In case 2, the inlet pressure in increased, which has the opposite effect. Here we compare case 1 to the base case; the trends are in the opposite direction when comparing case 2 to the base case.

The impact ionization rate is then decreased as a result of lower collision frequencies between the electrons and neutral species. This leads to a decrease in the plasma density and hence the current densities of the ions at the cathode and the electrons at the anode. The secondary emitted electron current density is decreased as well, due to the reduced ion influx to the cathode surface. The difference of the thermionic emission current density is attributed to the decreased electric field at the cathode surface (the Schottky effect, see equation 1), which is a consequence of the decreased charged particle density at the reduced background pressure.

With a decreasing background pressure, the collision frequency between the neutral species and electrons and therefore the loss of electron energy are decreased. Electrons are accelerated under the driving force of the applied field with a larger mean free path and can reach higher average energy as they propagate towards the anode, leading to a higher electron power deposition density at the anode. In contrast, a decrease in the background pressure leads to a decrease in the power delivered by the ion flux to the cathode. This occurs due to a decrease in the plasma density inside the cathode and hence the ion influx to the cathode.

2) Effect of discharge voltage

Comparing case 3 with base case, one can see that by increasing the discharge voltage from 750 V to 1000 V, the distance required for the electrons to acquire sufficient energy to ionize the gas is decreased. This leads to faster formation of the plasma at that location and to an increase in the plasma density as well as the electron and ion fluxes towards the anode and cathode respectively. This leads to an increase in the current density of the ions at the cathode and the electrons at the anode as well as the secondary-emitted electron current density and the discharge power deposition density at the cathode and anode surfaces. A similar dependence of discharge current on discharge voltage was obtained with a fluid model [20]. The results indicate that the microdischarge operates in an abnormal glow mode with positive differential resistivity.

3) Effect of work function

There exist large variations of the work function of aluminium/aluminium oxide in the literature, due to different manufacturing processes. Therefore, it is important to investigate the influence of the cathode work function on discharge properties. From the Richardson–Dushman equation, one can see that decreasing the cathode work function from 2.0 eV to 1.5 eV will increase the current density carried by the emitted electrons. Hence, the plasma density, current density and power density all increase correspondingly. With a value of the cathode work function of 4.0 eV, the thermionic emission of electrons and hence the thermionically-emitted electron current density at the cathode surface are negligible. This means that the emitted electrons from the cathode are only produced by the secondary electron emission effect. Under this condition, the maximum ion number density reduces to below 40% of that of the base case. Correspondingly, the ion current density and the power deposition density at the cathode decrease. In contrast, the electron current density and the electron power deposition density at the anode surface are increased. This occurs because the discharge core moves upstream inside the anode region, leading to an increase in the local plasma density and hence the electron power deposition density.

The lack of plasma parameters by experimental makes it difficult to validate our model by direct comparison under specific conditions. However, our calculated value for plasma density is comparable with experimental data from literature. For example, the magnitude of the peak electron densities predicted by the model for case 2 (6.54×10^{19} m^{-3}) is of the same order as the available quantitative experimental data for the MHCD using argon under a similar condition [14]. Moreover, the plasma density predicted by our model increases with the background pressure and discharge current. This trend is qualitatively in agreement with experimental investigation by the reference of [14].

5 Conclusions

A computational investigation of a micro-hollow cathode discharge using argon as the propellant in a prototypical micro plasma thruster (MPT) with a hollow cylinder geometry was conducted in the high-pressure (several hundreds of torr), high-current (mA) operating regime using a self-consistent two-dimensional Particle-in-cell/Monte-Carlo collision (PIC/MCC) model. The model takes into account thermionic electron emission including the Schottky effect, secondary electron emission due to cathode bombardment by the plasma ions, as well as several different collision processes including both elastic and inelastic interactions. The simulation calculates the evolution of the discharge parameters, and allows one to determine the typical discharge properties, including the distribution of plasma density and electric field, as well as average species energies in the different discharge stages. Emphasis was placed on the influence of the diverging nozzle shape and the non-uniform argon background gas density in the cathode–anode gap caused by the pressure difference between the inlet and outlet. The behaviour of cathode material sputter and the thermalization process of the sputtered atoms are described. The effects of different argon gas pressures, the cathode work function and discharge voltage on the operation of the microdischarge thruster are presented. The model is validated by comparing some of the obtained simulation results with the experimental data available in the literature, indicating that our computational scheme is reliable. Indeed, our calculated plasma density and average electron energy as well as larger plasma diameter outside the thruster shows a reasonable agreement with the experimental work at similar conditions. The dependence of plasma density on pressure and current also agree well with the experimental results.

Our results shows that the discharge processes may be separated into four different stages. In the first stage, before 50 ns, the electrons emitted from the cathodes are accelerated under the driving force of the electric field and there are almost no bulk electrons produced by impact ionization. Therefore, the initial electric potential and electric field distribution are hardly affected in this stage. In the second stage, in the time range from 50 ns to 100 ns, the electrons emitted from the cathode obtain enough energy from the electric field for impact ionization to occur; this takes place mainly in the region near the diverging nozzle, $x = [500, 600]\ \mu m$, leading to rapid increase in the electron number density in this region. The total number of electrons and ions in the discharge passage experiences a very rapid increase and the electric potential and the electric field distribution are slightly changed. In the third stage, from 100 ns to 280 ns, the bulk electrons produced by the impact ionization are further accelerated by the electric field and propagate towards the anodes, near which they react with the neutral argon gas. A second discharge core is generated in the anode region $x = [0, 150]\ \mu m$. For the second time, the total number of electrons and ions experiences a rapid increase. On the one hand, the increasing ion concentration can increase the electric potential in the cathode region and hence the ion fluxes towards the cathode. Therefore, the secondary electron emission effect as a result of the cathode bombardment by the plasma ions becomes important in this stage as a result of an increased ion impact on the cathode surface. On the other hand, a shallow well-shaped distribution of electric potential along the axial direction inside the cathode region can prevent the ions propagating out of the thruster. At t = 300 ns, a steady discharge is reached and the plasma properties do not vary with time.

Although the concentration of secondary electrons is minor compared to that of the thermionically-emitted electrons, the secondary electron emission effect was found to affect the discharge current as well as the power deposition density at the cathode and anode surfaces. Specifically, the calculated discharge current and the power deposition density are increased when the SEE effect is considered.

The diverging nozzle shape produces a radial component of the applied electric field that drives ions to propagate rapidly towards the cathode surface. As a result, the concentration and the average energy of ions increases with distance from the central axis towards the cathode surface at different axial locations. Additionally, the axial distributions of the density and the mean energy of ions bombarding the cathode internal surface decrease in the downstream direction. This explains the decreasing trend of the concentration of sputtered atoms in the downstream direction. Our work indicates the sputtered atoms are almost completely thermalized at a point $75\ \mu m$ away from the cathode.

The simulation results showed significant deviations of the electron energy distribution from a Maxwellian. Also, it was shown that the energy of ions accelerating inside the cathode sheath can reach tens of eV, which can lead to fast erosion of the cathode; an erosion rate of $0.152\ \mu m/h$ at the cathode surface is predicted.

The increase in gas pressure leads to an increase in the plasma density and hence the current density of the ions at the cathode and the electrons at the anode. The current density associated with thermionically- and secondary-emitted electrons is increased as well. The power deposition density of the ions at the cathode is increased due to the higher ion flux. In contrast, the power deposition density of the electrons at the anode is decreased as a result of the increased collision frequency between electrons and neutral species and hence electron energy loss.

The increase in the discharge voltage leads to the faster formation of the plasma inside the hollow discharge channel and hence an increase in the current densities as well as the power deposition densities at the cathode and anode. The current densities associated with the thermionically- and secondary-emitted electrons are also increased. This tendency indicates that the microdischarge operates in an abnormal glow mode with positive differential resistivity. This is in agreement with results presented in the literature.

A lower value of the work function of the cathode material leads to a higher density of the thermionically-emitted electrons and hence higher current densities as well as the power deposition densities at the cathode and anode. However, a higher work function, which leads to a negligible contribution of the thermionically-emitted electrons, can also lead to an increased electron current density and electron power deposition density at the anode surface. This occurs because the discharge core moves upstream inside the anode part, and leading to an increase in the local plasma density and hence the electron power deposition density.

Our current work provides a detailed understanding of physical and chemical mechanisms associated with direct current microdischarge phenomena occurring in a prototype MPT system. It is anticipated that the fundamental insights provided by this study can be used in the development and optimization of plasma-based micro thruster concepts for space propulsion application.

Acknowledgments

This work was supported by National Natural Science Foundation of China (Grant No. 51407182), Beijing Municipal Natural Science Foundation (Grant No. 3154044), the open project of State Key Laboratory of Electrical Insulation and Power Equipment (Grant No.EIPE14208), along with Innovative research fund and Internship project of Qian Xuesen Laboratory of Space Technology. The authors would like to acknowledge Dr Wei Jiang for his kind help and valuable discussions. These authors Linghan Kong and Weizong Wang contributed equally to this work.

Reference

[1] R. E. Bruce, "Introduction to satellite communication," 3rd Edition Book, Arctech House, 685, Canton Street, Norwood, MA 02062, 2008.

[2] P. Misra and P. Enge, "Global positioning system: signals, measurements, and performance," Lincoln, MA. : Ganga-Jamuna Press, 2001.

[3] R. W. Spencer and J. R. Christy, "Precise monitoring of global temperature trends from satellites,"

Science, Vol.247, 1558, 1990.

[4] J. C. Huang, J. H. Ji, and P. J. Ye, "The Ginger-shaped Asteroid 4179 Toutatis: New observations from a successful flyby of Chang'E-2," *Nature—Scientific Reports*, Vol. 3, 3411, 2013.

[5] C. D. Brown, Spacecraft propulsion, American Institute of Aeronautics and Astronautics, Washington, DC, 1996.

[6] M. M. Micci and A. D. Ketsdever, "Micropropulsion for Small Spacecraft," *Progress in Astronautics and Aeronautics*, Vol. 187, AIAA Inc., Reston, VA, 2000.

[7] C. Xie, "Characteristics of micronozzle gas flows," *Physics of Fluids*, Vol.19, 037102, 2007.

[8] A. A. Alexeenko, D. A. Levin, S. F. Gimelshein, R. J. Collins, and B. D. Reed, "Numerical modeling of axisymmetric and three-dimensional flows in microelectromechanical system nozzles," *AIAA Journal*, Vol.40, 2002.

[9] K. L. Williams, A. B. Eriksson, R. Thorslund, J. Kohler, M. Boman and L. Stenmark, "Numerical Modeling of axisymmetric and three-dimensional flows in microelectromechanical system nozzles," *Journal of Micromechanics and Microengineering*, Vol.16, 1, 2006.

[10] C. Charles, "Plasmas for spacecraft propulsion," *Journal of physics D: Applied Physics*, Vol.42, 163001, 2009.

[11] W. Z. Wang, L. H. Kong, J. Y. Geng, F. Z. Wei and G. Q. Xia, "Wall ablation of heated compound-materials into non-equilibrium discharge plasmas," *Journal of Physics D: Applied Physics,* 50, 074005, 2017.

[12] K. H. Becker, K. H. Schoenbach, and J. G. Eden, "Microplasmas and applications," *Journal of Physics D: Applied Physics*, Vol.39, R55, 2006.

[13] U. KC., J. Bingaman, P. L. Varghese, and L. L. Raja, "Studies of a direct-current microdischarge based miniaturized plasma thruster," *Progress in Propulsion Physics*, Vol.1, 399, 2009.

[14] G. Q. Xia, G. W. Mao and M. L. Chen, "Theoretical and experimental investigation of microhollow cathode discharge for the application to micro plasma thrusters," Proceeding of the 31st International Electric Propulsion Conference, IEPC-2009-028, University of Michigan, USA, September 20 – 24, 2009.

[15] R. L. Burton et al., "Initial development of the microcavity discharge thruster," in Proceeding of the 31st Internation Electric Propulsion Conference, Ann Arbor, Michigan, 2009.

[16] R. L. Burton et al., "Development of the MCD thruster for nanosat propulsion," in Proceedings of the 57th Joint Army Navy NASA Air Force Propulsion Meeting, Colorado Springs, Colorado, 2010.

[17] C. Penache, M. Miclea, A. Brauning-Demian, O. Hohn, S. Schossler, T. Jahnke, K. Niemax, and H. Schmidt-Bocking, "Characterization of a high-pressure microdischarge using diode laser atomic absorption spectroscopy, " *Plasma Sources Science and Technology,* 11, 476, 2002.

[18] F. Leipold, R. H. Stark, A. El-Habachi, and K. H. Schoenbach, "Electron density measurements in an atmospheric pressure air plasma by means of infrared heterodyne interferometry," *Journal of Physics D: Applied Physics*, 33, 2268, 2000.

[19] P. S. Kothnor, and L. L. Raja, "Simulation of direct-current microdischarges for application in electro-thermal class of small satellite propulsion devices," *Contribution to Plasma Physics*, Vol.47, 9, 2007.

[20] T. Deconick, S. Mahadevan, and L. L. Raja, "Computational simulation of coupled nonequilibrium discharge and compressible flow phenomena in a microplasma thruster," *Journal of Applied Physics,* Vol.106, 063305, 2009.

[21] Z. Chen, and A. Bogaerts, "Laser ablation of Cu and plume expansion into 1 atm ambient gas," *Journal of Physics,* Vol.97, 063305, 2005.

[22] Y. Zhang. W. Jiang and A. Bogaerts, "Kinetic simulation of direct-current driven microdischarges in argon at atmospheric pressure,' *Journal of Physics D: Applied Physics,* Vol. 47, 435201, 2014.

[23] W. Jiang, Y. Zhang and A. Bogaerts, "Numerical characterization of local electrical breakdown in sub-micrometer metallized film capacitors," *New Journal of Phys*ics, Vol.16, 113036, 2014.

[24] D. Levko, Ya. E. Krasik, V. Vekselman, and I. Haber, "Two-dimensional model of orificed micro-hollow cathode discharge for space application," *Physics of Plasmas*, Vol.20 (8), 083512, 2013.

[25] D. Levko, Y. P. Bliokh, and Ya. E. Krasik, "Influence of Xe_2^+ ions on the micro-hollow cathode discharge driven by thermionic emission," *Physics of Plasmas*, Vol. 21, 043503, 2014.

[26] D. Levko and Ya. E. Krasik, "Electron heating during discharges driven by thermionic emission," *Physics of Plasmas*, Vol. 21, 112105, 2014.

[27] A. Semnani, A. Venkattraman, A. A. Alexeenko, and D. Peroulis, "Pre-breakdown evaluation of gas discharge mechanisms in microgaps," *Applied Physics Letter*, Vol.102, 174102, 2013.

[28] F. Crawford, and S. Gabriel, "Modelling small hollow cathode discharges for ion microthrusters," *Proceeding* of *33rd Plasma dynamics and Lasers Conference,* AIAA2002-2101, *Hawaii, USA,* 20 - 23 May 2002.

[29] J. Choi, F. Iza, J. K. Lee, and C. M. Ryu, "Electron and ion kinetics in a DC microplasma at atmospheric pressure," *IEEE Transaction on Plasma Science*, Vol.35, 1274, 2007.

[30] G. J. Kim, F. Iza, and J. K. Lee, "Electron and ion kinetics in a micro hollow cathode discharge," *Journal of Physics D: Applied Physics,* Vol.39, 4386, 2006.

[31] G. J. Kim and J. K. Lee, "Pendulum electrons in micro hollow cathode discharges," *IEEE Transaction on Plasma Science*, Vol. 36, 1238, 2008.

[32] D. Goebel and I. Katz, *Fundamentals of Electric Propulsion*, John Wiley & Sons, 2008.

[33] J. Antula, "Work function aluminum-aluminum oxide Solid," *State Electronics*, Vol.9, 825, 1966.

[34] S. S. Yang, S. M. Lee, F. Iza and J. K. Lee, "Secondary electron emission coefficients in plasma display panels as determined by particle and fluid simulations," *Journal of physics D: Applied Physics*, Vol. 39, 2775, 2006.

[35] A. Bogaerts A and R. Gijbels, "The ion- and atom-induced secondary electron emission yield: numerical study for the effect of clean and dirty cathode surfaces," *Plasma Sources Science and Technology*, Vol. 11, 27, 2012.

[36] Bohdansky J and Roth J, "An analytical formula and important parameters for low-energy ion sputtering," *Journal of Applied physics*, Vol.51, 2861, 1980.

[37] N. Matsunami, Y. Yamamura, Y. Itikawa, N. Itoh, Y. Kazumata, S. Miyagawa , K. Morita, R. Shimizu, and H. Tawara, "Energy dependence of the ion-induced sputtering yields of monatomic solids," *Atomic Data & Nuclear Data Tables*, Vol. 31,1, 1984.

[38] V. Vahedi and M. Surendra, "A Monte Carlo collision model for the particle-in-cell method: Applications to argon and oxygen discharges," *Computer Physics Communications*, Vol. 87, 179, 1995.

[39] Y. Buckman, and A. V. Phelps, "Measurement of free–free emission from low-energy-electron collisions with Ar," *Phys. Rev. A*, Vol. 27, 1345, 1983

[40] D. Vender, R.W. Boswell, "Numerical modeling of low-pressure rf plasmas," *IEEE Transaction on Plasma Science*, Vol.18, 725, 1990.

[41] J. O. Hirschfelder, C. F. Curtis and R. B. Bird 1964 Molecular Theory of Gases and Liquids 2nd edn (New York: Wiley)

[42] A. Bogaerts, R. Gijbels, W.J. Goedheer, "Description of the thermalization process of the sputtered atoms in a glow discharge using a three-dimensional Monte Carlo method," *Journal of Applied physics*, Vol.77, 1868, 1995.

[43] S.-J. Park, K. S. Kim, and J. G. Eden, "Nanoporous alumina as a dielectric for microcavity plasma devices: multilayer Al/Al_2O_3 structures," *Applied Physics Letters*, Vol. 86, No. 22, 2005.

[44] R. Temam, "Navier–Stokes equations, theory and numerical analysis," AMS Chelsea, pp. 107–112, 2001.

[45] C. K. Birdsall and A. B. Langdon, Plasma Physics via Computer Simulation (IOP Publishing, Bristol, 1991).

[46] P. S. Kothnur and L. L. Raja, "Two-dimensional simulation of a direct-current microhollow cathode discharge," *Journal of Applied Physics*, 97, 043305, 2005.

[47] J. W. Frame, D. J. Wheeler, T. A. DeTemple, and J. G. Eden, "Hollow cathode sustained plasma microjets: Characterization and application to diamond deposition," *Applied Physics Letters*, 71, 1165, 1997.